

Cross-Domain Transfer with Self-Supervised Spectral-Spatial Modeling for Hyperspectral Image Classification

Jianshu Chao^{a,b}, Tianhua Lv^{c,d}, Qiqiong Ma^{c,d}, Yunfei Qiu^c, Li Fang^d,
Huifang Shen^{a,b,*}, Wei Yao^d

^a*Quanzhou Institute of Equipment Manufacturing, Haixi Institutes, Chinese Academy of Sciences, Quanzhou, China*

^b*Fujian Institute of Research on the Structure of Matter, Chinese Academy of Sciences, Fuzhou, China*

^c*Liaoning Technical University, Huludao, Liaoning, China*

^d*State Key Laboratory of Regional and Urban Ecology, Institute of Urban Environment, Chinese Academy of Sciences, Xiamen, China*

Abstract

Self-supervised learning has demonstrated considerable potential in hyperspectral representation, yet its application in cross-domain transfer scenarios remains under-explored. Existing methods, however, still rely on source domain annotations and are susceptible to distribution shifts, leading to degraded generalization performance in the target domain. To address this, this paper proposes a self-supervised cross-domain transfer framework that learns transferable spectral-spatial joint representations without source labels and achieves efficient adaptation under few samples in the target domain. During the self-supervised pre-training phase, a Spatial-Spectral Transformer (S²Former) module is designed. It adopts a dual-branch spatial-spectral transformer and introduces a bidirectional cross-attention mechanism to achieve spectral-spatial collaborative modeling: the spatial branch enhances structural awareness through random masking, while the spectral branch cap-

*This work was supported in part by the Supporting Project of the STS Program of the Chinese Academy of Sciences in Fujian Province under Grant 2024T3008, and in part by the Basic Scientific Research Project of the Education Department of Liaoning Province (Key Project of Independent Topic Selection, 2024) under Grant 524053218.

^{*}Corresponding author

Email address: `shenhf@fjirsm.ac.cn` (Huifang Shen)

tures fine-grained differences. Both branches mutually guide each other to improve semantic consistency. We further propose a Frequency Domain Constraint (FDC) to maintain frequency-domain consistency through real Fast Fourier Transform (rFFT) and high-frequency magnitude loss, thereby enhancing the model’s capability to discern fine details and boundaries. During the fine-tuning phase, we introduce a Diffusion-Aligned Fine-tuning (DAFT) distillation mechanism. This aligns semantic evolution trajectories through a teacher-student structure, enabling robust transfer learning under low-label conditions. Experimental results demonstrate stable classification performance and strong cross-domain adaptability across four hyperspectral datasets, validating the method’s effectiveness under resource-constrained conditions.

Keywords: Self-supervised learning, Few-shot cross-domain transfer learning, Hyperspectral image classification, Frequency domain consistency, Diffusion distillation

1. Introduction

Characterized by reflectance acquisition in numerous consecutive narrow spectral bands (Kumar et al., 2024), hyperspectral imagery (HSI) provides dense spectral-spatial information that has been extensively leveraged in precision agriculture, mineral exploration, environmental monitoring, and diverse remote sensing domains (Wang et al., 2023; Song et al., 2025; Ahmad et al., 2025).

In recent, deep learning has driven profound progress in hyperspectral image classification (HSIC) (Chen et al., 2014; Paoletti et al., 2019), with convolutional neural networks (CNNs) (Makantasis et al., 2015), 3D-CNNs (Zhang et al., 2020), and Transformer architectures (Fang et al., 2025) exhibiting strong feature representational power under sufficient annotations. For instance, SSTN (Zhong et al., 2022) boosts performance through self-attention and multi-scale integration in supervised settings (Shi et al., 2022). Nevertheless, these supervised approaches are strongly reliant on massive labeled samples (Polewski et al., 2016; Wang and Yao, 2022). The prohibitive annotation costs and low efficiency consequently restrict their practical deployment in data-scarce environment (Zhao et al., 2022).

With rising interest in reducing annotation reliance, self-supervised learning (SSL) has gained prominence (Chen et al., 2023; Khemiri et al., 2025),

with two primary paradigms emerging: masked modeling and contrastive learning (Liang et al., 2025). The former includes approaches such as SS-MAE (Lin et al., 2023), which randomly masks spatial and spectral regions to force contextual representation learning; S^2HM^2 (Tu et al., 2024), incorporating hierarchical masking combined with spectral angular error; and SSLSM (Liu et al., 2023), simulating spectral correlations through band prediction. The latter encompasses S3L (Guo and Liu, 2024), integrating multi-view consistent Transformers; self-supervised low-rank priors (He et al., 2025), compressing redundancy through spectral low-rank priors; $S^4L\text{-FSC}$ (Chen et al., 2025) and ES2FL (Liu et al., 2022), employing class-aware contrastive learning and multiple augmentation strategies respectively to enhance discriminative capability and intra-class consistency. These methods have achieved remarkable progress in homogeneous domain scenarios (Wambugu et al., 2021).

However, significant distribution discrepancies (domain shifts) arise between different hyperspectral data sources due to varying imaging conditions, sensor specifications, and geographical contexts, severely compromising model generalization in new domains (Wang et al., 2025; Huang et al., 2020). Traditional domain adaptation (DA) methods typically achieve unsupervised transfer via sample reweighting, feature alignment, or adversarial training, as exemplified by MMD (Long et al., 2015), and DANN (Ganin et al., 2016). These adaptation paradigms are gaining traction in HSIC for handling distribution shifts across multi-source scenarios (Zhou et al., 2023). For instance, MLUDA achieves joint alignment across pixel, feature, and logical levels, enhancing transfer performance through guided filtering and cross-attention (Wu et al., 2025); S4DL (Feng et al., 2025) introduces spectral-spatial decoupling and reversible structures to model inter-domain shifts. Open-Set DA algorithm addresses unknown class challenges by incorporating weighted generative adversarial networks with dynamic thresholding strategies (Zhang et al., 2025); DCFSL (Li et al., 2022) minimizes feature space discrepancies between source and target domains to enhance transferability; FDFSL (Qin et al., 2024) improves robustness in cross-domain few-shot learning through feature alignment strategies; HyMuT (Liu et al., 2024) employs multimodal fusion combining spectral and spatial features to enhance model adaptability in complex cross-domain scenarios. Although these approaches advance transfer performance, they still suffer from insufficient semantic modeling and limited transferability under extremely low-label conditions (Pan et al., 2017).

Emerging solutions hybridize reconstruction mechanisms, contrastive learn-

ing, and distillation strategies for hyperspectral cross-domain transfer (Chen et al., 2023). DEMA (Li et al., 2024) unifies masked modeling and diffusion processes, demonstrating strong discriminative capability and generalization performance under few-shot conditions through joint pre-training of reconstruction and diffusion. MSDDA (Fang et al., 2024) introduces mask-assisted reconstruction and semantic consistency distillation, improving feature alignment stability and discriminative power; CDnet (Lee and Kwon, 2022) constructs positive–negative sample pairs via cross-image contrastive learning, achieving preliminary self-supervised alignment in multi-source scenarios, effectively mitigating the label scarcity problem in target domain. Additionally, CTF (Xi et al., 2024) integrates semi-supervised and few-shot learning to enhance model performance under scarce label conditions. Despite these advances, feature alignment robustness and representation transferability persist as bottlenecks in complex cross-domain environments (Li et al., 2023; Thota and Leontidis, 2021).

Therefore, this paper proposes a self-supervised cross-domain transfer framework for HSIC that learns transferable spectral–spatial joint representations independent of source annotations, addressing key limitations of label dependency and generalization gaps in cross-domain HSIC (Chopra et al., 2023; Zhang and Han, 2023). It integrates self-supervised spectral–spatial synergy with diffusion-based semantic alignment for effective few-shot adaptation. Experimental evaluations confirm notable improvements in boundary sensitivity, semantic consistency, and cross-domain generalization.

The principal innovations of this paper are stated as follows:

- (1) A self-supervised cross-domain classification framework is proposed, which combines masked modeling with frequency-domain awareness during pre-training, allowing it to learn transferable spectral–spatial representations for lightweight adaptation with minimal target samples.
- (2) A Spatial-Spectral Transformer (S^2 Former) module is designed, which integrates spatial masking and spectral guidance in a dual-branch Transformer architecture, using bidirectional cross-attention for collaborative spectral–spatial modeling.
- (3) A Frequency Domain Constraint (FDC) is introduced, which leverages real Fast Fourier Transform (rFFT) and frequency band masking to construct a high-frequency mask loss, which enhances the model’s

capacity to capture spectral details and boosts its cross-domain discriminability.

(4) A Diffusion-Aligned Fine-tuning (DAFT) distillation mechanism is developed to construct a Diffusion trajectory aggregation loss, guiding the student model to learn the teacher's semantic evolution path in the target domain and mitigate semantic drift.

The subsequent sections are arranged in the following order. Section 2 details the proposed framework. Section 3 evaluates the method on several public datasets. Section 4 provides conclusions and future directions.

2. Methodology

As illustrated in Figure 1, our framework comprises four coordinated stages of spectral-spatial processing. Its core includes three specialized modules: S²Former for joint spatial-spectral dual-stream modeling, FDC for spectral enhancement, and DAFT for cross-domain adaptation.

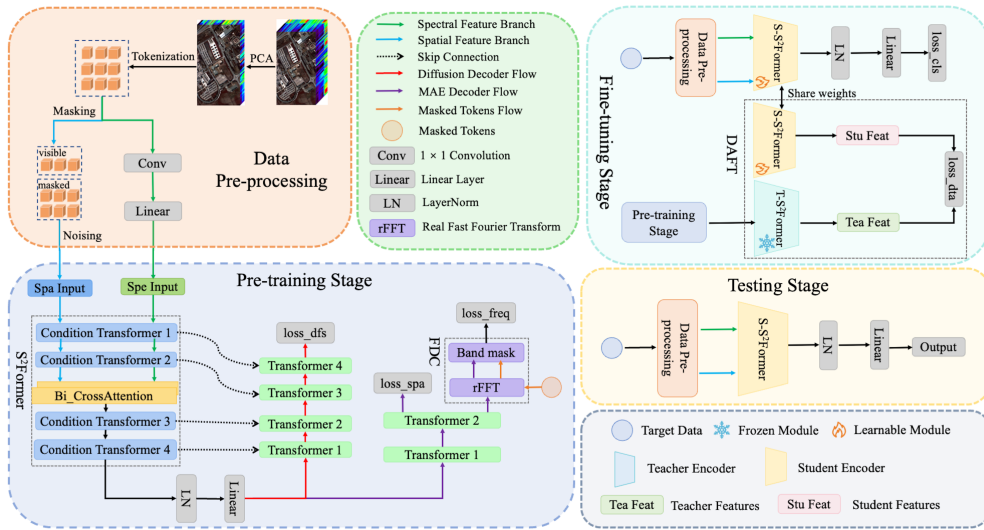


Figure 1: Overview of the proposed self-supervised cross-domain framework, encompassing four stages: data pre-processing, self-supervised pre-training, few-shot cross-domain fine-tuning, and testing.

Building upon DEMAЕ’s conditional transformer and noise processing paradigm, our framework enhances temporal token denoising through a learnable normalization layer (Adaptive Norm) with radial parametric generation (α/β), as shown in Figure 2. By integrating Markov-based noise injection with an inter-layer skip connected transformer decoder, the model achieves robust noise immunity and feature recovery.

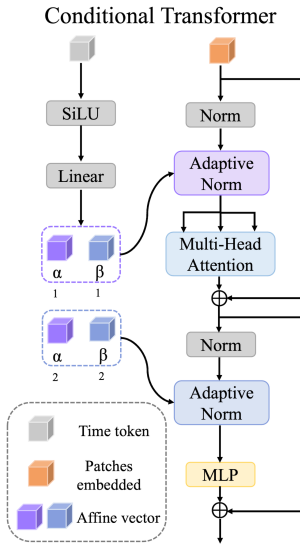


Figure 2: Condition transformer model (Li et al., 2024)

2.1. *S²Former (Spatial-Spectral Transformer)*

S²Former employs a four-layer conditional transformer architecture. The first two layers use parallel spatial-spectral dual-branch to capture local spatial context and spectral distribution characteristics, respectively, while the intermediate layer applies bidirectional cross-attention mechanism for deep cross-modal complementarity.

2.1.1. *Input modeling and encoding path*

As depicted in Figure 1, the pre-processing stage applies principal component analysis (PCA) to produce $\mathbf{X} \in \mathbb{R}^{H \times W \times C}$, followed by segmentation into $p \times p$ patches that are rearranged into a token sequence \mathbf{S} for mini-batch training:

$$\mathbf{S} = [\mathbf{s}_1, \mathbf{s}_2, \dots, \mathbf{s}_N]^\top \in \mathbb{R}^{B \times N \times C}, \quad N = \frac{H \cdot W}{p^2}, \quad (1)$$

where H , W and C denote the height, width, and spectral dimension of \mathbf{X} , respectively. B denotes the batch size. N represents the number of tokens, with each token $\mathbf{s}_n (n = 1, \dots, N)$ corresponding to a $p \times p$ image patch.

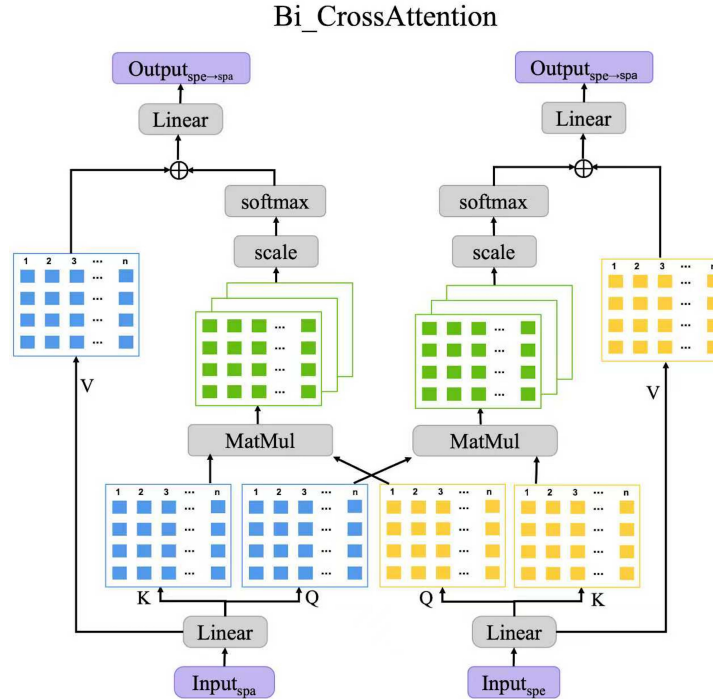


Figure 3: Bidirectional Cross-Attention Module

Next, two decoupled encoding branches are constructed:

1) Spatial branch

The spatial branch randomly masks each token at a preset ratio, dividing them into $X_{\text{spa}}^{\text{vis}}$ and $X_{\text{spa}}^{\text{mask}}$, then adds the diffusion time encoding $\mathbf{T} \in \mathbb{R}^{1 \times D}$ to $X_{\text{spa}}^{\text{vis}}$.

$$\mathbf{Z}_{\text{spa}}^{(0)} = \mathbf{X}_{\text{spa}}^{\text{vis}} \cdot \mathbf{W}_{\text{spa}} + \mathbf{T}, \quad \mathbf{W}_{\text{spa}} \in \mathbb{R}^{C \times D}, \quad (2)$$

where $\mathbf{Z}_{\text{spa}}^{(0)} \in \mathbb{R}^{B \times N_{\text{vis}} \times D}$ is the spatial feature sequence, with N_{vis} and D

representing the visible token count and feature dimension, and \mathbf{W}_{spa} the spatial embedding matrix.

The sequence $\mathbf{Z}_{\text{spa}}^{(0)}$ undergoes hierarchical feature transformation through two conditional transformer encoders.

$$\mathbf{Z}_{\text{spa}}^{(l)} = \text{CTransformer}(\mathbf{Z}_{\text{spa}}^{(l-1)}) \quad (l = 1, 2), \quad (3)$$

where $\text{CTransformer}(\cdot)$ denotes the conditional transformer, $\mathbf{Z}_{\text{spa}}^{(l)}$ the current layer output, and $\mathbf{Z}_{\text{spa}}^{(l-1)}$ the previous layer input.

2) Spectral branch

The spectral branch applies 1D convolution along the spectral dimension to process mini-batched tokens \mathbf{S} .

$$\hat{\mathbf{X}}_{\text{spec}} = \text{Conv1D}(\mathbf{S}; \mathbf{W}_{\text{conv}}), \quad (4)$$

where $\mathbf{W}_{\text{conv}} \in \mathbb{R}^{K \times C}$ is the convolution kernel with size K .

Subsequent linear projection maps each token's spectral features to the target feature space.

$$\mathbf{X}_{\text{spec}} = \text{Linear}(\hat{\mathbf{X}}_{\text{spec}}; \mathbf{W}_{\text{spec}}), \quad (5)$$

where $\mathbf{W}_{\text{spec}} \in \mathbb{R}^{C \times D}$ is the projection matrix.

Diffusion time encoding $\mathbf{T} \in \mathbb{R}^{1 \times D}$ is then added into the spectral features, yielding the final spectral feature sequence $\mathbf{Z}_{\text{spec}}^{(0)} \in \mathbb{R}^{B \times N \times D}$:

$$\mathbf{Z}_{\text{spec}}^{(0)} = \mathbf{X}_{\text{spec}} + \mathbf{T}. \quad (6)$$

Spectral features pass through two conditional transformer layers, evolving from $\mathbf{Z}_{\text{spec}}^{(0)}$ into $\mathbf{Z}_{\text{spec}}^{(2)}$.

2.1.2. Bidirectional cross-attention

Our encoder utilizes bidirectional cross-attention (Figure 3) for dual interaction and cross-modal fusion.

1) Spectral-to-spatial

First, spectral tokens $\mathbf{Z}_{\text{spec}}^{(2)} \in \mathbb{R}^{B \times N \times D}$ are averaged by:

$$\bar{\mathbf{Z}}_{\text{spec}} = \frac{1}{N} \sum_{i=1}^N \mathbf{Z}_{\text{spec}}^{(2)(i)}. \quad (7)$$

Proceed to form the cross-attention inputs:

$$\mathbf{Q} = \mathbf{Z}_{\text{spa}}^{(2)} \cdot \mathbf{W}_Q, \quad \mathbf{K} = \bar{\mathbf{Z}}_{\text{spec}} \cdot \mathbf{W}_K, \quad \mathbf{V} = \bar{\mathbf{Z}}_{\text{spec}} \cdot \mathbf{W}_V, \quad (8)$$

where $\mathbf{W}_Q, \mathbf{W}_K, \mathbf{W}_V \in \mathbb{R}^{D \times d}$ are projection matrices, and d is the attention head dimension.

The frequency-guided spatial attention is defined as:

$$\text{Attn}_{\text{spa}} = \text{Softmax} \left(\frac{\mathbf{Q}\mathbf{K}^\top}{\sqrt{d}} \right) \mathbf{V}. \quad (9)$$

Then, the fusion residual is expressed as:

$$\hat{\mathbf{Z}}_{\text{spa}} = \mathbf{Z}_{\text{spa}}^{(2)} + \text{Attn}_{\text{spa}}. \quad (10)$$

This spectral-guided mechanism directs the spatial pathway to focus on spectral-sensitive regions, achieving complementary feature enhancement.

2) Spatial-to-spectral

Similarly, mean pooling aggregates the spatial representation:

$$\bar{\mathbf{Z}}_{\text{spa}} = \frac{1}{N_{\text{vis}}} \sum_{i=1}^{N_{\text{vis}}} \mathbf{Z}_{\text{spa}}^{(2)(i)} \quad (11)$$

Construct spectral attention inputs:

$$\mathbf{Q} = \mathbf{Z}_{\text{spec}}^{(2)} \cdot \mathbf{W}'_Q, \quad \mathbf{K} = \bar{\mathbf{Z}}_{\text{spa}} \cdot \mathbf{W}'_K, \quad \mathbf{V} = \bar{\mathbf{Z}}_{\text{spa}} \cdot \mathbf{W}'_V, \quad (12)$$

where $\mathbf{W}'_Q, \mathbf{W}'_K, \mathbf{W}'_V \in \mathbb{R}^{D \times d}$ are the attention mapping matrices.

Thus, yielding the spatial-guided spectral attention output:

$$\text{Attn}_{\text{spec}} = \text{Softmax} \left(\frac{\mathbf{Q}\mathbf{K}^\top}{\sqrt{d}} \right) \mathbf{V}. \quad (13)$$

The fusion residual in this direction is represented as:

$$\hat{\mathbf{Z}}_{\text{spec}} = \mathbf{Z}_{\text{spec}}^{(2)} + \text{Attn}_{\text{spec}}. \quad (14)$$

The cross-attention refined spatial features $\hat{\mathbf{Z}}_{\text{spa}}$ and spectral features $\hat{\mathbf{Z}}_{\text{spec}}$ are concatenated and linearly transformation into a unified representation:

$$\hat{\mathbf{Z}}_{\text{fuse}} = \text{Linear} \left(\text{concat} \left[\hat{\mathbf{Z}}_{\text{spa}}, \hat{\mathbf{Z}}_{\text{spec}} \right] \right). \quad (15)$$

Subsequently, $\hat{\mathbf{Z}}_{\text{fuse}}$ undergoes feature refinement via two conditional transformer layers, followed by LayerNorm and linear layer, to generate enhanced features \mathbf{Z}_{fuse} for subsequent tasks.

2.2. Frequency-Domain Constraint (FDC)

To improve the model’s ability to capture fine-grained spectral features in hyperspectral images, this paper introduces a Frequency-Domain Constraint (FDC) during the self-supervised pre-training phase, as shown in Figure 1. This module employs explicit spectral-domain supervision to guide the model toward focusing on high-frequency components at masked locations, thereby enhancing its representational capacity and cross-domain generalization performance.

The reconstruction decoder initializes the sequence by placing \mathbf{Z}_{fuse} at visible positions and learnable tokens $\mathbf{M}_{\text{mask}}^{\text{init}}$ at masked regions. After adding shared positional embedding \mathbf{P} to all tokens to form $\mathbf{X}_{\text{dec}}^{(0)}$, a two-layer transformer decoder processes it to generate the final output \mathbf{X}_{dec} , where the reconstructed features $\hat{\mathbf{X}}_{\text{spa}}^{\text{mask}}$ are extracted from masked positions.

To evaluate spectral restoration in the frequency domain, we apply the rFFT to both reconstructed $\hat{\mathbf{X}}_{\text{spa}}^{\text{mask}}$ and ground-truth $\mathbf{X}_{\text{spa}}^{\text{mask}}$:

$$\tilde{\mathbf{X}}_{\text{freq},n} = \mathcal{F}_r(\mathbf{X}_{\text{spa},n}^{\text{mask}}), \quad \hat{\tilde{\mathbf{X}}}_{\text{freq},n} = \mathcal{F}_r(\hat{\mathbf{X}}_{\text{spa},n}^{\text{mask}}), \quad \forall n \in \mathcal{M}, \quad (16)$$

where $\mathcal{M} \in \{1, \dots, M\}$ is the masked token set, with $\mathbf{X}_{\text{spa},n}^{\text{mask}}$ and $\hat{\mathbf{X}}_{\text{spa},n}^{\text{mask}}$ being the ground-truth and predicted value at the n -th masked position. The rFFT operation $\mathcal{F}_r(\cdot)$ along the channel dimension produces a complex spectrum of dimension $C' = \lfloor C/2 \rfloor + 1$.

To emphasize high-frequency components, we employ a frequency band mask $\mathbf{m} \in \{0, 1\}^{C'}$ defined as:

$$\mathbf{m}_i = \begin{cases} 1, & \text{if } i > \tau C' \\ 0, & \text{otherwise} \end{cases} \quad \text{with } \tau \in (0, 1), \quad (17)$$

where τ controls the high-frequency band’s start ($\tau = 0.3$), $i \in \{0, 1, \dots, C' - 1\}$ denotes the frequency channel index. $\mathbf{m}_i = 1$ selects high-frequency components for loss calculation, while $\mathbf{m}_i = 0$ excludes low-frequency channels.

2.3. Diffusion-Aligned Fine-tuning (DAFT)

This paper proposes Diffusion-Aligned Fine-tuning (DAFT), using a frozen source-domain teacher to guide a target-domain student through a tripartite joint loss (classification, timestep alignment, and distillation consistency) for stable few-shot transfer (Figure 1).

An input sample \mathbf{X} is partitioned into tokens S , then perturbed with diffusion noise at a random timestep $t \in \mathcal{K}, \mathcal{K} = \{1, 2, \dots, T_S\}$, where T_S represents the total diffusion steps.

$$\mathbf{x}^{(t)} = \sqrt{\bar{\alpha}_t} \cdot \mathbf{x} + \sqrt{1 - \bar{\alpha}_t} \cdot \epsilon, \quad \epsilon \sim N(0, \mathbf{I}), \quad (18)$$

where $\bar{\alpha}_t$ denotes the cumulative retention factor and ϵ represents standard Gaussian noise, and \mathbf{x} refers to the token-level representation sampled from the token sequence \mathbf{S} .

At timestep t , the teacher \mathbf{f}_T and student \mathbf{f}_S respectively output features:

$$\mathbf{z}_T^{(t)} = \mathbf{f}_T(\mathbf{x}^{(t)}), \quad \mathbf{z}_S^{(t)} = \mathbf{f}_S(\mathbf{x}^{(t)}), \quad (19)$$

where $\mathbf{z}_T^{(t)}$ and $\mathbf{z}_S^{(t)}$ are the class tokens from the teacher and student models at timestep t , used for measuring their feature consistency within the diffusion semantic space.

2.4. Loss functions

To enhance the model's generalization and cross-domain adaptability, we design multiple loss functions for joint optimization during both pre-training and fine-tuning.

2.4.1. Pre-training losses

The pre-training phase optimizes the encoder through self-supervision using two primary objective functions.

1) Signal-guided classification loss

The masked reconstruction branch loss combines spatial and frequency-domain constraint term to guide encoder reconstruction of both spatial structures and spectral features.

The spatial reconstruction term employs a pointwise ℓ_1 loss:

$$\mathcal{L}_{\text{spa}} = \frac{1}{|\mathcal{M}|} \sum_{n \in \mathcal{M}} \left\| \hat{\mathbf{X}}_{\text{spa},n}^{\text{mask}} - \mathbf{X}_{\text{spa},n}^{\text{mask}} \right\|_1. \quad (20)$$

The frequency-domain reconstruction term is formulated as:

$$\mathcal{L}_{\text{freq}} = \frac{1}{|\mathcal{M}|} \sum_{n \in \mathcal{M}} \left\| \mathbf{m} \odot \left(|\tilde{\mathbf{X}}_{\text{freq},n}| - |\hat{\mathbf{X}}_{\text{freq},n}| \right) \right\|_1, \quad (21)$$

where $|\cdot|$ and \odot denote spectral magnitude and element-wise multiplication, constraining the model to preserve accurate distributions in high-frequency regions and thereby enhancing its sensitivity to fine-grained spectral differences.

The reconstruction loss is given by:

$$\mathcal{L}_{\text{recon}} = \mathcal{L}_{\text{spa}} + \alpha \cdot \mathcal{L}_{\text{freq}}, \quad (22)$$

where the hyperparameter $\alpha \in \mathbb{R}^+$ controls the importance of frequency-domain supervision (typically 0.5).

2) Diffusion loss (DFS loss)

Depicted in Figure 1, a four-layer diffusion decoder processes \mathbf{Z}_{fuse} with encoder skip connections, outputting denoised visible features $\hat{\mathbf{X}}_{\text{vis}}$ that are evaluated against clean targets $\mathbf{X}_{\text{spa}}^{\text{vis}}$ via mean squared error (MSE) loss:

$$\mathcal{L}_{\text{dfs}} = \text{MSE}\left(\mathbf{X}_{\text{spa}}^{\text{vis}}, \hat{\mathbf{X}}_{\text{vis}}\right) = \left\| \hat{\mathbf{X}}_{\text{vis}} - \mathbf{X}_{\text{spa}}^{\text{vis}} \right\|_2^2. \quad (23)$$

Overall, the final pre-training loss is:

$$\mathcal{L}_{\text{pretrain}} = \mathcal{L}_{\text{recon}} + \mathcal{L}_{\text{dfs}}. \quad (24)$$

The two equally weighted losses balance reconstruction of masked spectral-spatial information with robust modeling of visible region perturbations.

2.4.2. Fine-tuning losses

Fine-tuning aims for strong discriminative and source-target consistency in the target domain, using two losses as specified below.

1) Signal-to-Noise Ratio-Enhanced classification loss (SNR-Enhanced loss)

To enhance model stability across SNR levels after diffusion perturbations, SNR-Enhanced loss is applied:

$$\mathcal{L}_{\text{cls}} = \text{SNREnhanced}(h(z_S^{(0)}), y, \text{SNR}), \quad (25)$$

where $h(\mathbf{z}_S^{(0)})$ represents the student's class token, with $z_S^{(0)}$ being the class token feature obtained from the diffusion-perturbed input, y is the ground truth, and SNR weights the loss by reducing the contribution of high-SNR (low-noise) samples and increasing that of low-SNR (high-noise) samples.

2) Diffusion Trajectory Aggregation loss

For cross-timestep semantic alignment, the feature consistency loss at each timestep t as:

$$\mathcal{L}_{cd}^{(t)} = 1 - \cos \left(\mathbf{f}_s^{(t)}, \mathbf{P} \left(\mathbf{f}_t^{(t)} \right) \right), \quad (26)$$

where $\mathbf{f}_s^{(t)} \in \mathbb{R}^{D_s}$ and $\mathbf{f}_t^{(t)} \in \mathbb{R}^{D_t}$ are student and teacher features at t , $\mathbf{P}(\cdot)$ is an optional projection for the mismatch of $\mathbf{f}_s^{(t)}$ and $\mathbf{f}_t^{(t)}$, and $\cos(\cdot, \cdot)$ represents cosine similarity.

Consequently, we introduce an aggregated loss to enforce globally consistent alignment of the feature trajectories across the entire time series:

$$\mathcal{L}_{dta} = \frac{1}{|\mathcal{K}|} \sum_{t \in \mathcal{K}} \left[1 - \cos \left(\mathbf{f}_s^{(t)}, \mathbf{P} \left(\mathbf{f}_t^{(t)} \right) \right) \right]. \quad (27)$$

Overall, the final fine-tuning loss is:

$$\mathcal{L}_{DAFT} = \mathcal{L}_{cls} + \lambda \cdot \mathcal{L}_{dta}. \quad (28)$$

where λ balances alignment and classification, ensuring the student adapts to the target domain while preserving source domain semantic knowledge.

3. Experimental results

3.1. Data description

For rigorous validation of cross-domain transfer capability in HSIC, we employ four benchmark datasets—Pavia Center (PC), Houston2013 (HU), Pavia University (PU), and Salinas (SA)—with Salinas excluding water vapor absorption bands. The selected datasets demonstrate heterogeneous characteristics across spectral details, spatial resolutions, land cover types, and sensor configurations, ensuring thorough assessment of domain adaptation performance. Key parameters of all datasets (size, band information, and labeled sample counts) are detailed in Table 1.

Table 1: Size, band information, and number of labeled samples per class for four datasets.

Datasets		PC		HU		PU		SA	
Size and bands		1096 × 715 × 102		512 × 217 × 204		610 × 340 × 103		349 × 1905 × 144	
Class	Name	Number		Name	Number	Name	Number	Name	Number
1	Water	824		Healthy grass	1251	Asphalt	6631	Brocoli green weeds 1	2009
2	Trees	820		Stressed grass	1254	Meadows	18649	Brocoli green weeds 2	3726
3	Asphalt	816		Synthetic grass	697	Gravel	2099	Fallow	1976
4	Bitumen	808		Trees	1244	Trees	3064	Fallow rough plow	1394
5	Bricks	808		Soil	1242	Painted metal sheets	1345	Fallow smooth	2678
6	Tiles	1260		Water	325	Bare soil	5029	Stubble	3959
7	Shadows	476		Residential	1268	Bitumen	1330	Celery	3579
8	Bare soil	824		Commercial	1244	Self-Blocking Bricks	3682	Grapes untrained	11271
9	Meadows	820		Road	1252	Shadows	947	Soil vineyard develop	6203
10				Highway	1227			Corn senesced green weeds	3278
11				Railway	1235			Lettuce romaine 4wk	1068
12				Parking Lot1	1233			Lettuce romaine 5wk	1927
13				Parking Lot2	469			Lettuce romaine 6wk	916
14				Tennis court	428			Lettuce romaine 7wk	1070
15				Running track	660			Vineyard untrained	7268
16								Vineyard vertical trellis	1807
	Total	7456		Total	15029	Total	42776	Total	54129

Transfer Tasks include the following scenarios:

- 1) **PU→PC:** Transfer from campus scenes (PU) to urban architecture (PC) using homologous ROSIS sensors (1.3m), testing adaptation from regular campus to complex urban scenes.
- 2) **SA→HU:** Cross-sensor transfer from agriculture SA (AVIRIS 3.7 m) to urban HU (ITRES CASI-1500 2.5m) with significant domain shifts, verifying robustness across sensor and land cover types.
- 3) **HU→PU:** Reverse transfer from complex urban HU to structured campus PU, evaluating model stabilization under distribution divergence.
- 4) **PC→SA:** Urban-to-agricultural transfer between PC (urban buildings) and SA (agricultural parcels) with distinct feature categories, background structures and spectral dimensions, assessing cross-landscape representation capability.

3.2. Experimental setup

Hyperparameter are set according to dataset-adaptive configurations during both pre-training and fine-tuning phases. Specifically, the PU dataset is trained for 200 epochs in both stages. For the SA dataset, pre-training uses 300 epochs and fine-tuning 250 epochs. The HU dataset uses 300 epochs for pre-training and 200 for fine-tuning, while the PC dataset adopts 300 and 200 epochs for pre-training and fine-tuning, respectively. Regarding the batch size, all datasets uniformly use a size of 512 during pre-training. In the fine-tuning phase, the batch size is adjusted per dataset: 45 for PU and PC, 80 for SA, and 75 for HU. For all datasets, the initial learning rate during

both pre-training and fine-tuning phases is fixed at 1×10^{-3} , with a masking ratio of 0.75. The noise scale is kept consistent across the two phases, set to $[1 \times 10^{-4}, 2 \times 10^{-2}]$, aligning with the classic settings of the DEMAЕ method. Additionally, a learning rate decay strategy with a decay factor of 0.99 per epoch is applied to ensure training stability.

The experimental sample configuration and performance evaluation design are implemented as follows: For fine-tuning, we randomly select 5 labeled samples per category for training and use the remainder reserved for testing. Evaluation employs Overall Accuracy (OA), Average Accuracy (AA), and Kappa Coefficient (κ), with results averaged over 10 independent runs (mean pm stand deviation). All experiments are executed on an RTX 3080 Ti GPU with PyTorch 1.10.0 and CUDA 11.3.

3.3. Classification results

We evaluate cross-domain classification with sparse labeled sample on the aforementioned four transfer tasks. Compared methods include: fully supervised SSTN(Zhong et al., 2022); few-shot semi-supervised CTF(Xi et al., 2024); self-supervised DEMAЕ(Li et al., 2024); and three cross-domain methods DCFSL(Li et al., 2022), FDFSL(Qin et al., 2024), HyMuT(Liu et al., 2024).

1) For the PU \rightarrow PC task (Table 2), our method achieves superior comprehensive performance with exceptional global recognition and local consistency. Quantitative results show that OA achieves 96.98% (+0.31% over DCFSL, +0.53% over DEMAЕ), AA reaches 93.30% (+0.71% over DEMAЕ, +1.92% over CTF), Kappa equals 95.73% (+0.73% over DEMAЕ, +0.43% DCFSL). Visually, it produces more coherent boundaries in complex regions (Figure 4), especially in urban-vegetation transitions.

2) For the challenging SA \rightarrow HU task with high spectral similarity and minimal material variation (Table 3), our model attains 79.88% OA, 82.89% AA, and 78.28% Kappa, gaining average approximately 2%–3% average improvement over DEMAЕ and CTF. It exhibits enhanced robustness in low-contrast regions, producing smoother boundaries and better structural detail preservation (Figure 5).

3) For the HU \rightarrow PU task presented in Table 4, our model delivers robust performance with 84.82% OA, 87.03% AA, and 80.44% Kappa, outperforming DEMAЕ and CTF. It excels in classifying spectral-variable features (Trees: 86.23%, Bare Soil: 99.90%), confirming robustness to shadow and

texture noise. Visual results (Figure 6) show precise vegetation and bare soil delineation with natural transitions and boundary continuity.

4) For the PC \rightarrow SA task with complex land cover and uneven distribution (Table 5), our method achieves 93.05% OA, 96.19% AA, and 92.28% Kappa, showing distinct advantage in discriminating spectrally similar categories. Despite DEMAЕ’s local representation capability and SSTN’s texture robustness, our approach overcomes their limitations in local fragmentation and boundary ambiguity. Visual results (Figure 7) confirm superior global consistency and balanced class representation.

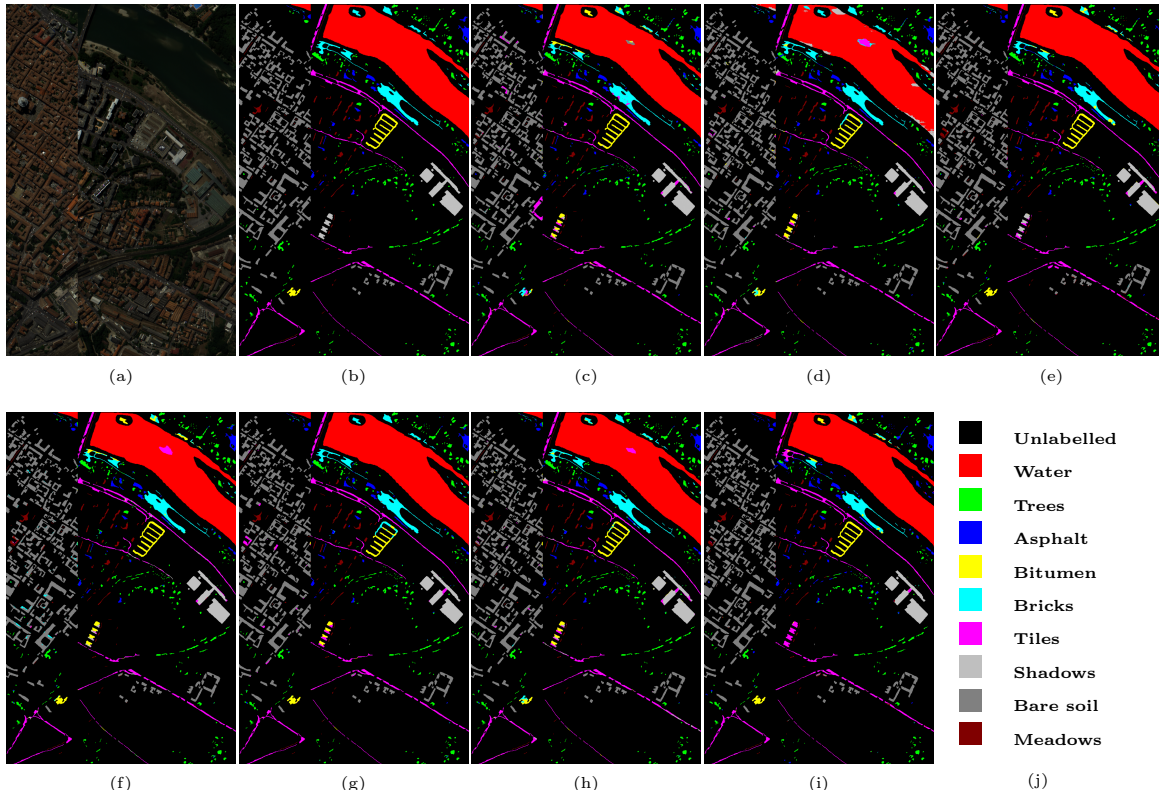


Figure 4: Classification maps of different methods on PU \rightarrow PC task. (a) False color image. (b) Ground-truth. (c) SSTN. (d) CTF. (e) DEMAЕ. (f) DCFSL. (g) FDFSL. (h) HyMuT. (i) Ours. (j) Color labels

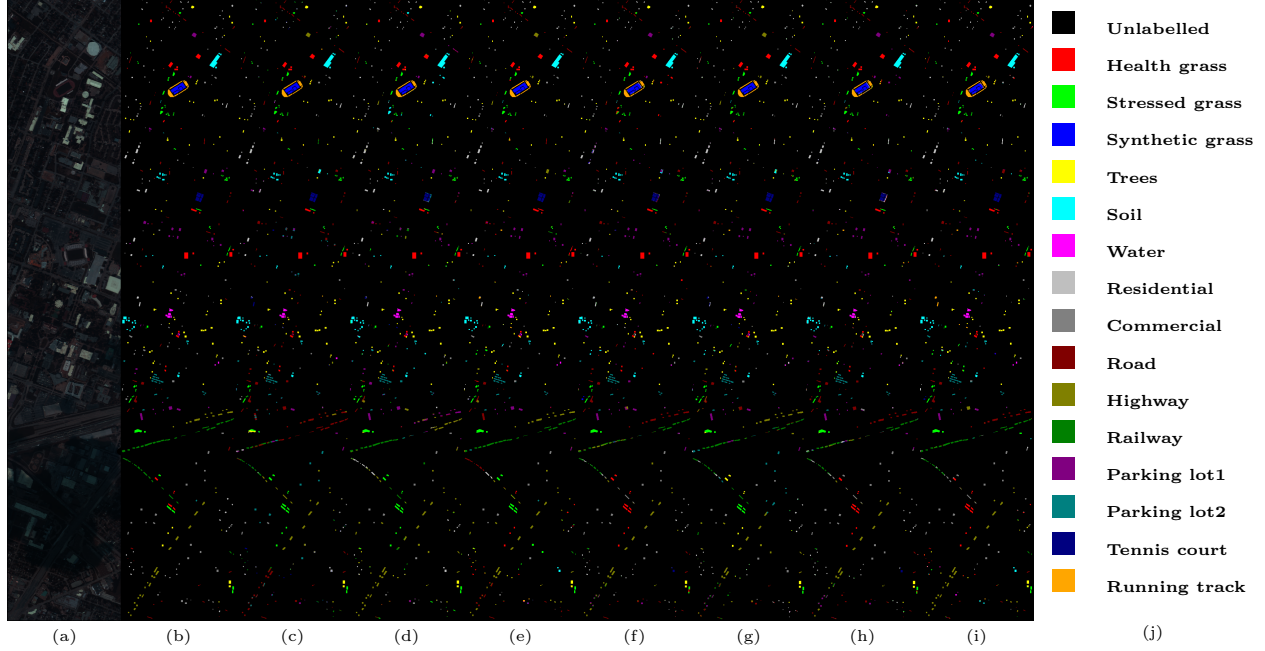


Figure 5: Classification maps of different methods on the SA→HU task. (a) False color image. (b) Ground-truth. (c) SSTN. (d) CTF. (e) DEMAЕ. (f) DCFSL. (g) FDFSL. (h) HyMuT. (i) Ours. (j) Color labels.

Table 2: Classification results on PU training – PC testing task

Metric	SSTN	CTF	DEMAЕ	DCFSL	FDFSL	HyMuT	Ours
1	95.76 ± 1.73	98.11 ± 1.33	99.50 ± 0.57	99.63 ± 0.17	98.76 ± 0.59	99.63 ± 0.26	99.98 ± 0.06
2	67.30 ± 23.64	85.25 ± 12.23	88.12 ± 4.98	90.25 ± 5.56	81.24 ± 4.74	90.35 ± 3.94	84.04 ± 7.24
3	94.17 ± 3.90	94.81 ± 1.84	85.82 ± 17.65	91.12 ± 2.19	80.19 ± 9.03	91.05 ± 5.77	94.71 ± 3.33
4	63.61 ± 16.52	86.49 ± 3.34	99.50 ± 0.71	96.23 ± 2.78	79.42 ± 18.66	89.40 ± 8.73	97.25 ± 2.96
5	91.26 ± 1.31	90.42 ± 5.47	82.66 ± 8.75	85.06 ± 3.27	76.07 ± 8.34	90.39 ± 5.82	87.52 ± 7.63
6	97.18 ± 1.66	95.65 ± 2.55	95.26 ± 4.16	95.66 ± 1.50	83.19 ± 8.90	90.43 ± 9.62	91.82 ± 8.86
7	90.95 ± 2.69	81.33 ± 4.68	88.99 ± 5.40	84.68 ± 2.34	79.76 ± 4.66	83.03 ± 1.94	91.99 ± 6.16
8	97.27 ± 1.35	94.42 ± 3.79	97.48 ± 2.80	97.54 ± 1.31	86.19 ± 8.37	97.17 ± 1.66	98.41 ± 1.33
9	96.29 ± 4.26	95.96 ± 1.69	95.92 ± 2.63	99.31 ± 1.06	92.15 ± 5.39	98.60 ± 0.85	94.00 ± 2.19
OA	93.80 ± 1.54	94.74 ± 1.56	96.45 ± 0.82	96.67 ± 0.61	90.45 ± 2.32	96.26 ± 0.26	96.98 ± 0.67
AA	88.26 ± 4.55	91.38 ± 2.59	92.59 ± 2.33	93.28 ± 0.55	84.11 ± 2.30	92.33 ± 1.76	93.30 ± 1.34
$\kappa \times 100$	91.33 ± 2.15	92.62 ± 2.20	95.00 ± 1.15	95.30 ± 0.85	86.71 ± 3.12	94.73 ± 1.20	95.73 ± 0.95

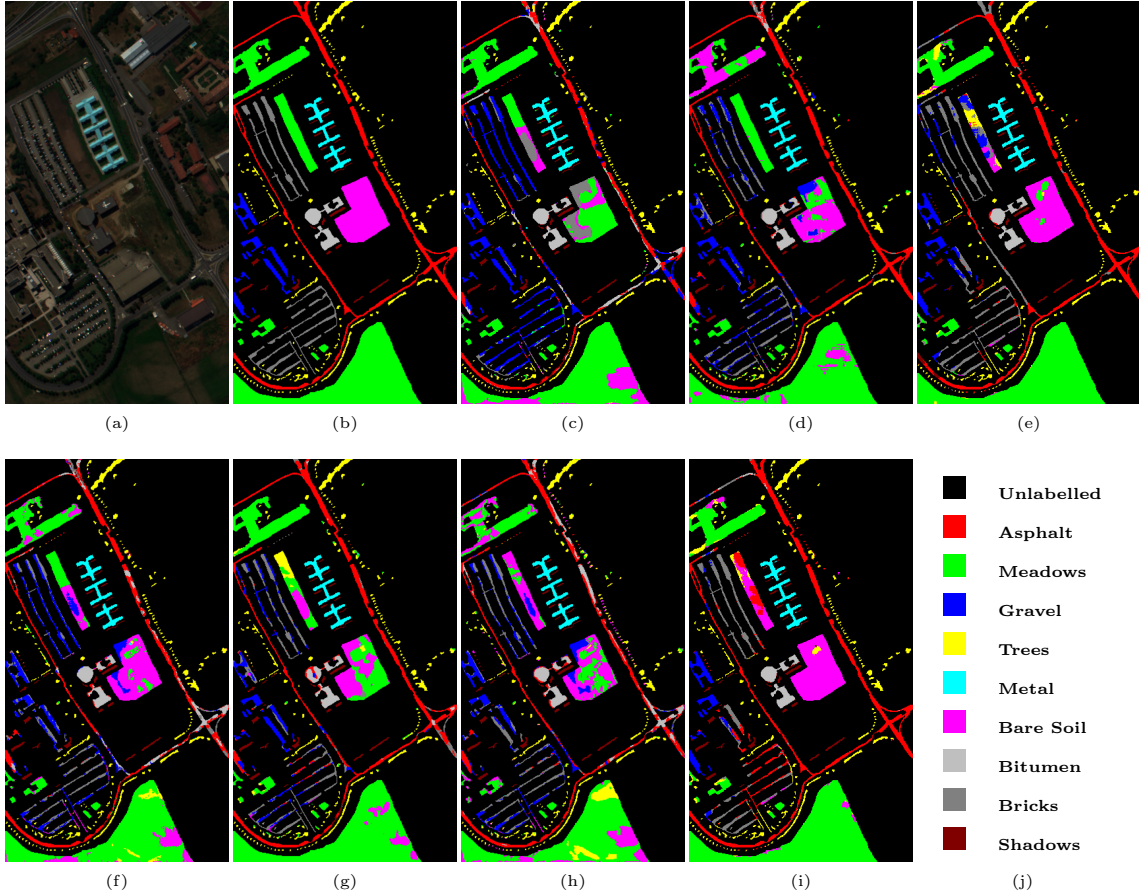


Figure 6: Classification maps of different methods on HU→PU task. (a) False color image. (b) Ground-truth. (c) SSTN. (d) CTF. (e) DEMAЕ. (f) DCFSL. (g) FDFSL. (h) HyMuT. (i) Ours. (j) Color labels

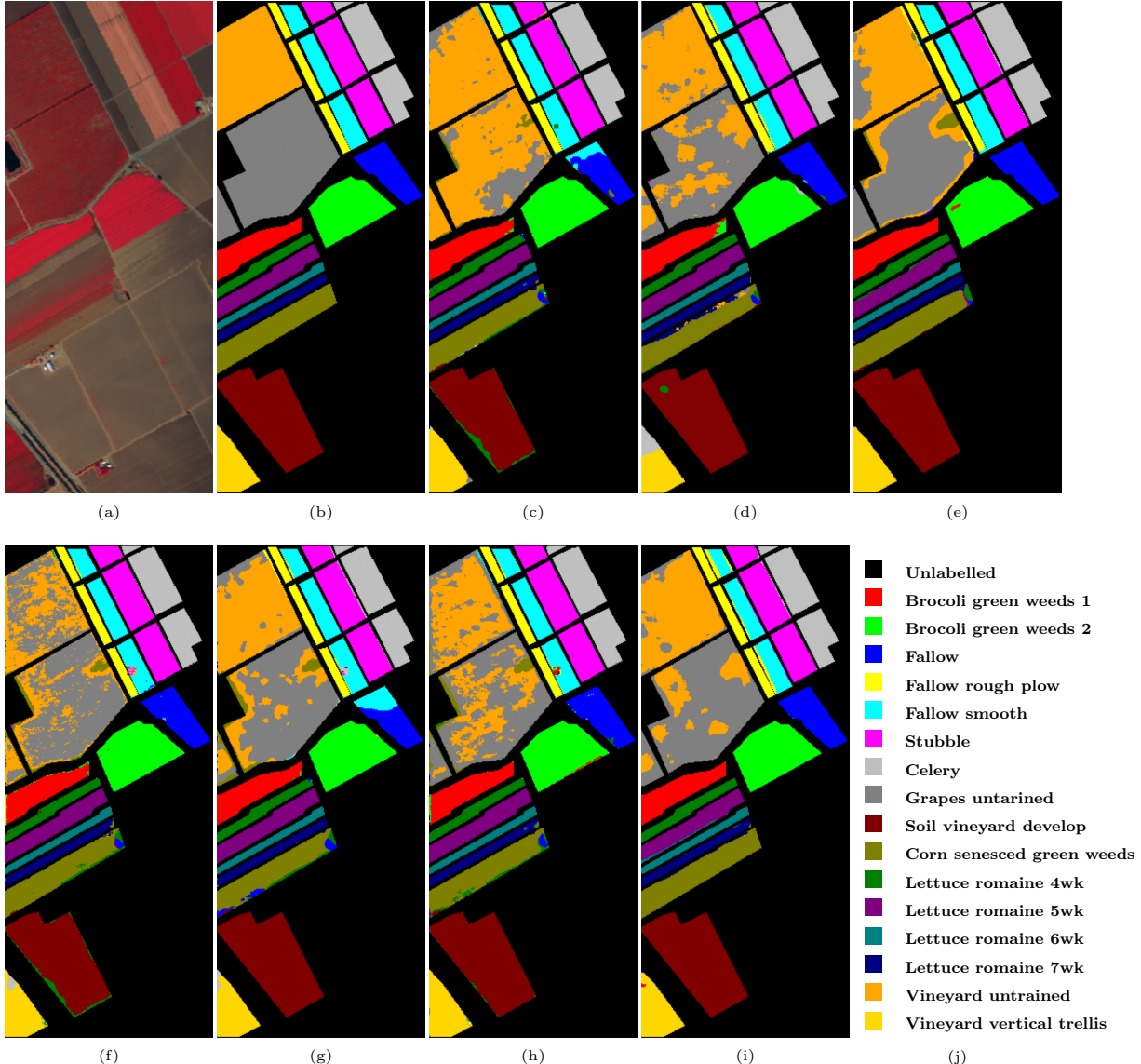


Figure 7: Classification maps of different methods on PC→SA task. (a) False color image. (b) Ground-truth. (c) SSTN. (d) CTF. (e) DEMAЕ. (f) DCFSL. (g) FDFSL. (h) HyMuT. (i) Ours. (j) Color labels

Table 3: Classification results on SA training – HU testing task

Metric	SSTN	CTF	DEMAE	DCFSL	FDFSL	HyMuT	Ours
1	81.02 \pm 5.04	89.62 \pm 7.36	80.22 \pm 10.45	90.22 \pm 6.42	84.09 \pm 5.36	90.27 \pm 6.64	82.89 \pm 10.23
2	76.63 \pm 13.89	74.81 \pm 7.78	87.89 \pm 6.56	81.44 \pm 9.89	73.34 \pm 12.52	81.41 \pm 3.31	88.06 \pm 5.07
3	99.95 \pm 0.07	98.70 \pm 1.64	98.34 \pm 1.78	94.77 \pm 3.38	88.86 \pm 7.86	96.24 \pm 2.92	97.11 \pm 3.25
4	93.82 \pm 0.43	90.93 \pm 0.83	85.87 \pm 6.85	90.02 \pm 3.86	78.65 \pm 4.15	90.14 \pm 2.68	85.56 \pm 4.83
5	93.34 \pm 7.12	93.86 \pm 7.68	99.79 \pm 0.48	94.86 \pm 4.35	87.96 \pm 6.38	98.67 \pm 0.89	99.83 \pm 0.39
6	83.83 \pm 3.01	86.56 \pm 4.51	92.25 \pm 6.23	76.25 \pm 3.39	68.94 \pm 4.84	74.81 \pm 4.59	90.69 \pm 3.69
7	60.07 \pm 12.22	79.47 \pm 5.10	65.23 \pm 15.28	72.46 \pm 14.71	53.09 \pm 9.74	67.25 \pm 13.04	65.90 \pm 10.38
8	13.81 \pm 8.55	44.15 \pm 11.65	48.48 \pm 8.03	34.50 \pm 3.50	40.61 \pm 9.64	40.31 \pm 6.80	47.36 \pm 8.60
9	76.76 \pm 12.22	77.17 \pm 8.37	69.25 \pm 9.14	60.45 \pm 17.11	69.94 \pm 7.42	77.32 \pm 6.41	64.61 \pm 9.17
10	33.50 \pm 5.00	60.97 \pm 8.76	74.06 \pm 16.75	60.03 \pm 9.53	58.88 \pm 12.28	55.73 \pm 17.12	78.44 \pm 13.88
11	56.49 \pm 24.74	57.07 \pm 8.66	81.95 \pm 13.58	58.18 \pm 5.26	48.49 \pm 8.29	61.11 \pm 8.18	75.76 \pm 12.10
12	17.04 \pm 4.97	70.85 \pm 2.21	60.68 \pm 10.07	70.54 \pm 5.58	45.68 \pm 8.93	63.99 \pm 9.33	76.53 \pm 12.40
13	38.98 \pm 32.77	92.17 \pm 2.43	86.47 \pm 8.90	90.99 \pm 2.80	80.60 \pm 8.75	87.11 \pm 9.07	92.44 \pm 3.80
14	99.18 \pm 0.99	91.88 \pm 7.53	100.00 \pm 0.00	91.63 \pm 3.75	85.60 \pm 8.10	88.09 \pm 7.53	99.91 \pm 0.22
15	99.79 \pm 0.29	98.37 \pm 0.88	99.56 \pm 0.87	92.95 \pm 6.66	87.05 \pm 5.37	95.15 \pm 3.05	99.15 \pm 2.03
OA	64.80 \pm 4.23	77.50 \pm 1.75	78.87 \pm 3.70	74.63 \pm 2.39	67.48 \pm 2.51	75.67 \pm 1.46	79.88 \pm 1.75
AA	68.28 \pm 3.83	80.44 \pm 1.76	82.00 \pm 3.18	77.29 \pm 1.99	70.12 \pm 2.37	77.84 \pm 0.70	82.89 \pm 1.35
$\kappa \times 100$	62.02 \pm 4.67	75.69 \pm 1.88	77.20 \pm 3.99	72.58 \pm 2.57	64.91 \pm 2.70	73.71 \pm 1.54	78.28 \pm 1.89

Table 4: Classification results on HU training – PU testing task

Metric	SSTN	CTF	DEMAE	DCFSL	FDFSL	HyMuT	Ours
1	74.46 \pm 8.53	83.20 \pm 6.12	72.46 \pm 8.64	89.57 \pm 6.43	62.43 \pm 11.08	77.64 \pm 15.63	77.74 \pm 9.10
2	54.67 \pm 18.14	65.05 \pm 14.52	85.46 \pm 7.93	78.77 \pm 10.59	68.69 \pm 7.75	78.71 \pm 6.91	86.23 \pm 7.02
3	64.73 \pm 29.69	67.19 \pm 12.43	81.00 \pm 11.10	98.15 \pm 1.81	50.34 \pm 12.98	61.45 \pm 11.00	83.56 \pm 7.68
4	89.84 \pm 3.03	87.88 \pm 3.19	87.59 \pm 3.84	88.56 \pm 4.72	80.91 \pm 8.48	90.83 \pm 4.27	90.15 \pm 3.79
5	98.77 \pm 1.74	99.65 \pm 0.18	99.57 \pm 0.59	96.41 \pm 4.34	98.54 \pm 0.98	96.09 \pm 3.47	99.90 \pm 0.21
6	60.04 \pm 31.67	91.67 \pm 4.92	90.70 \pm 6.80	79.50 \pm 2.57	57.90 \pm 8.15	66.48 \pm 16.12	87.64 \pm 6.79
7	96.31 \pm 0.94	96.91 \pm 0.79	96.95 \pm 2.00	74.90 \pm 12.34	65.42 \pm 12.08	79.14 \pm 8.79	97.54 \pm 1.63
8	45.59 \pm 35.66	78.73 \pm 14.66	77.02 \pm 9.25	41.29 \pm 4.59	51.56 \pm 11.13	65.29 \pm 18.62	71.86 \pm 13.47
9	94.71 \pm 3.61	99.01 \pm 0.52	87.14 \pm 9.26	70.28 \pm 9.77	88.51 \pm 7.81	99.41 \pm 0.43	88.62 \pm 9.22
OA	64.21 \pm 3.18	76.73 \pm 5.62	84.10 \pm 2.76	76.72 \pm 1.82	66.22 \pm 3.52	76.99 \pm 4.31	84.82 \pm 2.94
AA	75.57 \pm 4.89	84.81 \pm 0.69	86.43 \pm 2.27	79.25 \pm 1.70	69.37 \pm 2.75	79.45 \pm 2.43	87.03 \pm 1.61
$\kappa \times 100$	55.99 \pm 3.14	71.14 \pm 6.13	79.55 \pm 3.23	74.83 \pm 1.97	57.29 \pm 3.81	70.40 \pm 5.14	80.44 \pm 3.51

Table 5: Classification results on PC training – SA testing task

Metric	SSTN	CTF	DEMAE	DCFSL	FDFSL	HyMuT	Ours
1	97.99 \pm 1.42	99.63 \pm 0.29	99.80 \pm 0.55	98.28 \pm 1.94	88.26 \pm 4.44	94.71 \pm 4.03	99.99 \pm 0.03
2	99.91 \pm 1.42	99.96 \pm 0.05	100.00 \pm 0.00	95.62 \pm 8.08	96.42 \pm 1.99	98.84 \pm 0.76	97.89 \pm 4.09
3	78.12 \pm 17.85	97.24 \pm 1.95	98.39 \pm 4.69	98.04 \pm 1.56	82.52 \pm 10.01	91.56 \pm 7.20	97.81 \pm 3.08
4	98.01 \pm 0.92	99.21 \pm 0.60	98.76 \pm 1.21	98.76 \pm 1.33	96.98 \pm 1.69	99.06 \pm 0.93	99.47 \pm 0.79
5	97.05 \pm 1.26	93.83 \pm 1.80	92.26 \pm 5.15	92.01 \pm 0.92	81.15 \pm 6.36	91.16 \pm 3.33	93.32 \pm 4.07
6	97.86 \pm 1.29	99.94 \pm 0.04	98.28 \pm 2.01	99.38 \pm 0.73	97.73 \pm 1.33	97.92 \pm 2.11	99.55 \pm 0.84
7	99.81 \pm 0.06	99.85 \pm 0.13	99.93 \pm 0.13	99.50 \pm 0.21	98.19 \pm 0.93	99.17 \pm 0.70	99.93 \pm 0.12
8	53.78 \pm 10.48	80.89 \pm 3.53	78.00 \pm 6.63	67.27 \pm 10.68	69.50 \pm 7.57	71.88 \pm 8.63	82.26 \pm 8.13
9	98.27 \pm 1.07	99.63 \pm 0.45	100.00 \pm 0.00	98.93 \pm 1.39	96.74 \pm 1.63	98.56 \pm 1.45	99.95 \pm 0.11
10	86.37 \pm 10.48	87.14 \pm 1.25	92.24 \pm 3.17	84.98 \pm 4.39	70.57 \pm 11.63	82.49 \pm 10.40	95.45 \pm 3.14
11	90.71 \pm 1.72	97.37 \pm 2.39	99.97 \pm 0.08	98.34 \pm 1.06	89.45 \pm 3.71	96.41 \pm 1.98	99.97 \pm 0.06
12	99.81 \pm 0.24	99.71 \pm 0.09	97.86 \pm 2.77	99.35 \pm 0.86	99.01 \pm 1.01	99.65 \pm 0.40	98.30 \pm 2.54
13	99.74 \pm 0.19	99.09 \pm 0.72	99.43 \pm 0.63	99.43 \pm 0.55	98.19 \pm 1.50	99.32 \pm 0.32	99.62 \pm 0.65
14	93.21 \pm 2.46	99.00 \pm 0.77	96.50 \pm 4.99	98.42 \pm 1.09	97.95 \pm 1.30	97.71 \pm 0.83	93.15 \pm 7.69
15	87.21 \pm 7.96	78.15 \pm 15.30	86.43 \pm 8.16	67.47 \pm 6.60	70.81 \pm 5.76	73.59 \pm 5.20	84.48 \pm 13.01
16	97.97 \pm 1.09	91.05 \pm 5.66	97.99 \pm 3.35	91.79 \pm 6.53	82.37 \pm 6.31	84.71 \pm 7.60	97.83 \pm 3.58
OA	85.96 \pm 1.90	91.41 \pm 1.59	92.29 \pm 0.93	86.46 \pm 2.30	84.05 \pm 1.51	87.46 \pm 1.25	93.05 \pm 0.65
AA	92.24 \pm 1.27	95.10 \pm 0.87	95.99 \pm 0.80	92.97 \pm 0.42	88.49 \pm 1.02	92.30 \pm 1.11	96.19 \pm 0.68
$\kappa \times 100$	84.47 \pm 2.06	90.44 \pm 1.78	91.44 \pm 1.03	84.97 \pm 2.52	82.30 \pm 1.64	86.07 \pm 1.37	92.28 \pm 0.72

3.4. Parameter Analysis

A systematic parameter analysis is performed, where comparative evaluation of classification performance across diverse parameter settings in cross-domain scenarios enables performance-based optimization.

1) Band masking ratio (*masking_ratio*)

The masking ratio critically affects spectral feature learning. Insufficient masking (ratio=0.1) weakens constraint effectiveness, whereas excessive masking (ratio=0.5) fractures spectral continuity. Quantitative evidence shows ratio elevation from 0.1 to 0.3 boosts SA→HU performance (OA +2.54%, AA +2.04%, and Kappa +2.74%), but further raising it to 0.5 degrades HU→PU metrics (OA -2.50%, AA -1.72%, Kappa -0.16%).

2) Number of bidirection cross-attention layers (*Bicrossattention_num*)

It directly determines the interaction capacity between spatial and spectral features in S²Former, which exhibits a non-monotonic relationship with model performance. The two-layer configuration represents the computational sweet spot, with 1→2 layer increase boosting HU→PU metrics by 0.99% OA, 1.15% AA and 1.28% Kappa, while 2→3 layer increase causes 3.25% OA, 2.98% AA and 4.08% Kappa degradation. Single-layer interactions inadequately activate complementary features, whereas three-layer design induces overparameterization. The two-layer architecture optimally

balances classification accuracy and stability.

3) Training Sample Size

The sample size scalability experiment examines cross-domain performance under varying target domain quantities (from 5 to 25 samples per class with 5-sample intervals). Under consistent experimental conditions, our method demonstrates progressive performance gains with increasing sample size across all transfer tasks, surpassing all comparative methods in sample efficiency.

Table 6: Performance comparison of different parameter settings

Source	Target	Metric	Masking_ratio			Bicrossattention_num		
			0.1	Ours (0.3)	0.5	1	Ours (2)	3
PU	PC	OA	96.18 \pm 0.85	96.98 \pm 0.67	96.63 \pm 0.61	96.71 \pm 1.03	96.98 \pm 0.67	96.35 \pm 0.99
		AA	91.87 \pm 1.77	93.30 \pm 1.34	92.73 \pm 1.50	92.98 \pm 1.87	93.30 \pm 1.34	92.75 \pm 1.53
		$\kappa \times 100$	94.61 \pm 1.20	95.73 \pm 0.95	95.24 \pm 0.86	95.35 \pm 1.44	95.73 \pm 0.95	94.85 \pm 1.39
SA	HU	OA	77.34 \pm 2.85	79.88 \pm 1.75	78.99 \pm 3.10	78.18 \pm 1.55	79.88 \pm 1.75	78.29 \pm 3.83
		AA	80.85 \pm 2.43	82.89 \pm 1.35	82.23 \pm 2.63	81.37 \pm 1.30	82.89 \pm 1.35	81.55 \pm 3.20
		$\kappa \times 100$	75.54 \pm 3.07	78.28 \pm 1.89	77.32 \pm 3.34	76.44 \pm 1.67	78.28 \pm 1.89	76.56 \pm 4.14
HU	PU	OA	83.36 \pm 3.51	84.82 \pm 2.94	82.32 \pm 3.39	83.83 \pm 4.23	84.82 \pm 2.94	81.57 \pm 3.22
		AA	86.33 \pm 1.40	87.03 \pm 1.61	85.31 \pm 2.19	85.88 \pm 3.10	87.03 \pm 1.61	84.05 \pm 2.95
		$\kappa \times 100$	78.65 \pm 4.07	80.44 \pm 3.51	77.28 \pm 3.91	79.16 \pm 5.09	80.44 \pm 3.51	76.36 \pm 3.85
PC	SA	OA	92.93 \pm 0.83	93.05 \pm 0.65	92.54 \pm 1.22	92.46 \pm 1.43	93.05 \pm 0.65	92.72 \pm 1.03
		AA	95.73 \pm 0.99	96.19 \pm 0.68	95.76 \pm 0.99	95.84 \pm 0.88	96.19 \pm 0.68	95.94 \pm 0.89
		$\kappa \times 100$	92.15 \pm 0.91	92.28 \pm 0.72	91.72 \pm 1.35	91.65 \pm 1.58	92.28 \pm 0.72	91.91 \pm 1.13

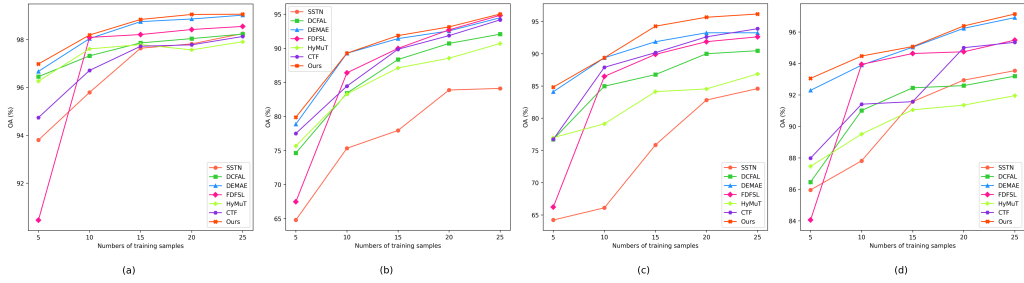


Figure 8: OA values for different sample sizes and models

3.5. Ablation experiments and visualization

Ablation experiments assessing module contributions sequentially remove S²Former, FDC, and DAFT module, comparing variants with the complete model across four tasks. The t-SNE visualizations reveal the feature clustering effects after data preprocessing and classification.

- 1) Ablating S²Former causes in the most severe performance deterioration, with HU→PU metrics dropping by 3.34% OA and 4.29% Kappa, with similar trends observed across other tasks. This confirms its indispensable spatial–spectral modeling capability. The module’s bidirectional attention mechanism enables dynamic fusion of spatial and spectral information, capturing both local patterns and global dependencies. Its removal cripples cross-modal integration, impairing feature alignment and classification accuracy.
- 2) FDC ablation demonstrates context-dependent effectiveness: it degrades performance in spectrally complex tasks (SA→HU: -1.14% OA, -1.23% Kappa, similar trends observed in PU→PC and PC→SA tasks) while slightly improving simpler scenarios (HU→PU: +0.34% OA, +0.22% Kappa). This contrast confirms FDC’s specialization in spectral detail preservation and high-frequency modeling for complex targets. The performance gain in HU→PU suggests feature smoothing benefits in structurally simple environments, revealing the module’s adaptive value based on spectral-structural complexity.
- 3) DAFT proves critical for domain alignment, with its removal causing severe performance drop in the HU→PU task (6.66% OA, 7.77% Kappa). The module enables cross-domain feature calibration through collaborative alignment, preventing semantic drift and maintaining distribution balance. Its absence disrupts transfer stability, confirming its role in domain adaption.
- 4) As shown in Figure 9, our model produces tightly clustered features and distinct boundaries in the target domain, successfully separating spectrally similar categories (e.g., categories 7 and 8 in PC, categories 2 and 5 in HU) and refining ambiguous categories (e.g., categories 8 and 10 in SA, categories 2 and 7 in PU) through improved intra-class clustering and inter-class separation after self-supervised transfer, demonstrating superior discriminative capability.

Table 7: Ablation study results between different modules

Source	Target	Metric	w/o S ² Former	w/o FDC	w/o DAFT	Ours
PU	PC	OA	96.01 \pm 1.10	96.29 \pm 1.21	96.32 \pm 1.20	96.98 \pm 0.67
		AA	91.56 \pm 1.21	92.07 \pm 2.38	92.49 \pm 1.46	93.30 \pm 1.34
		$\kappa \times 100$	94.37 \pm 1.53	94.77 \pm 1.68	94.82 \pm 1.65	95.73 \pm 0.95
SA	HU	OA	77.20 \pm 2.21	78.74 \pm 1.24	78.06 \pm 2.99	79.88 \pm 1.75
		AA	80.53 \pm 1.76	81.81 \pm 1.08	81.26 \pm 2.56	82.89 \pm 1.35
		$\kappa \times 100$	75.38 \pm 2.29	77.05 \pm 1.33	76.31 \pm 3.23	78.28 \pm 1.89
HU	PU	OA	81.48 \pm 1.59	85.16 \pm 2.36	78.16 \pm 5.15	84.82 \pm 2.94
		AA	81.70 \pm 1.16	85.86 \pm 2.40	84.73 \pm 2.04	87.03 \pm 1.61
		$\kappa \times 100$	76.15 \pm 1.94	80.66 \pm 3.03	72.67 \pm 5.74	80.44 \pm 3.51
PC	SA	OA	92.26 \pm 0.72	92.79 \pm 0.31	92.17 \pm 0.63	93.05 \pm 0.65
		AA	96.02 \pm 0.77	95.87 \pm 0.81	95.44 \pm 1.00	96.19 \pm 0.68
		$\kappa \times 100$	91.41 \pm 0.80	91.99 \pm 0.34	91.30 \pm 0.70	92.28 \pm 0.72

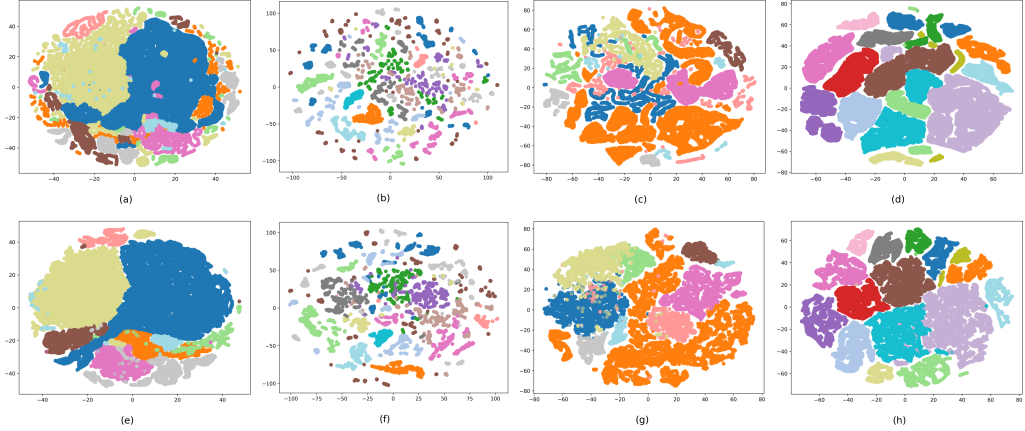


Figure 9: t-SNE visualization of the preprocessing and classification features on four target domain datasets. (a) PC dataset after preprocessing, (b) HU dataset after preprocessing, (c) PU dataset after preprocessing, (d) SA dataset after preprocessing. (e) PC dataset after classification, (f) HU dataset after classification, (g) PU dataset after classification, (h) SA dataset after classification.

4. Conclusion

A novel self-supervised cross-domain transfer framework is proposed in this paper, which successfully addresses the challenge of cross-domain transfer in hyperspectral image classification by learning transferable spectral-spatial joint representations without label supervision. For self-supervised

pre-training, the designed S²Former module incorporates dual-branch transformer operating on spatial and spectral domains, enhanced by bidirectional cross-attention for effective spectral-spatial cooperative modeling. The spatial branch enhances structural awareness through random masking, while the spectral branch captures fine-grained differences. These branches mutually guide each other to improve semantic consistency. The FDC strengthens the model’s capacity to discern details and boundaries by preserving frequency-domain structural consistency. During fine-tuning, the proposed DAFT mechanism effectively aligns semantic evolution trajectories, enabling robust transfer learning under low-label conditions.

Experimental results indicate stable classification performance and excellent cross-domain adaptability across four hyperspectral datasets, confirming its efficacy under resource-constrained conditions. Nevertheless, the current approach focuses solely on pre-existing semantic features in the target domain. Future research could explore specific characteristics of unlabeled data within the target domain through self-supervised methods like contrastive learning to substantially improve cross-domain transfer resilience and adaptive performance.

References

Ahmad, M., Distefano, S., Khan, A.M., Mazzara, M., Li, C., Li, H., Aryal, J., Ding, Y., Vivone, G., Hong, D., 2025. A comprehensive survey for hyperspectral image classification: The evolution from conventional to transformers and mamba models. *Neurocomputing* 644, 130428. doi:10.1016/j.neucom.2025.130428.

Chen, L., Wu, J., Xie, Y., Chen, E., Zhang, X., 2023. Discriminative feature constraints via supervised contrastive learning for few-shot forest tree species classification using airborne hyperspectral images. *Remote Sens. Environ.* 295, 113710. doi:10.1016/j.rse.2023.113710.

Chen, W., Zhang, Y., Xiao, Z., Chu, J., Wang, X., 2025. Spectral-spatial self-supervised learning for few-shot hyperspectral image classification. *arXiv preprint*. doi:10.48550/arXiv.2505.12482.

Chen, Y., Lin, Z., Zhao, X., Wang, G., Gu, Y., 2014. Deep learning-based classification of hyperspectral data. *IEEE J. Sel. Top. Appl. Earth Obs. Remote Sens.* 7, 2094–2107. doi:10.1109/JSTARS.2014.2329330.

Chopra, M., Chhipa, P.C., Mengi, G., Gupta, V., Liwicki, M., 2023. Domain adaptable self-supervised representation learning on remote sensing satellite imagery, in: Proc. Int. Joint Conf. Neural Netw. (IJCNN), pp. 1–8. doi:10.1109/IJCNN54540.2023.10191249.

Fang, L., Lan, X., Li, T., Shen, H., 2025. Pct: Patch confidence-enhanced transformer with efficient spectral–spatial features for hyperspectral image classification. *Int. J. Appl. Earth Observ. Geoinf.* 136, 104308. doi:10.1016/j.jag.2024.104308.

Fang, Z., He, W., Li, Z., Du, Q., Chen, Q., 2024. Masked self-distillation domain adaptation for hyperspectral image classification. *IEEE Trans. Geosci. Remote Sens.* 62, 1–20. doi:10.1109/TGRS.2024.3436814.

Feng, J., Zhang, T., Zhang, J., Shang, R., Dong, W., Shi, G., Jiao, L., 2025. *S⁴DL*: Shift-sensitive spatial–spectral disentangling learning for hyperspectral image unsupervised domain adaptation. *IEEE Trans. Neural Netw. Learn. Syst.* 36. doi:10.1109/tnnls.2025.3556386.

Ganin, Y., Ustinova, E., Ajakan, H., Germain, P., Larochelle, H., Laviolette, F., March, M., Lempitsky, V., 2016. Domain-adversarial training of neural networks. *J. Mach. Learn. Res.* 17, 1–35.

Guo, H., Liu, W., 2024. S3l: Spectrum transformer for self-supervised learning in hyperspectral image classification. *Remote Sens.* 16, 970. doi:10.3390/rs16060970.

He, Z., Wang, L., Meng, Z., Yuan, X., 2025. Self-supervised learning with spectral low-rank prior for hyperspectral image reconstruction, in: Proc. IEEE Winter Conf. Appl. Comput. Vis. (WACV), pp. 9136–9145. doi:10.1109/WACV61041.2025.00885.

Huang, R., Xu, Y., Hong, D., Yao, W., Ghamisi, P., Stilla, U., 2020. Deep point embedding for urban classification using als point clouds: A new perspective from local to global. *ISPRS J. Photogramm. Remote Sens.* 163, 62–81.

Khemiri, C., Inoubli, W., Farah, M., 2025. Deep contrastive graph learning framework for hyperspectral image classification. *Procedia Comput. Sci.* 270, 3588–3597. doi:10.1016/j.procs.2025.09.484.

Kumar, V., Singh, R.S., Rambabu, M., Dua, Y., 2024. Deep learning for hyperspectral image classification: A survey. *Comput. Sci. Rev.* 53, 100658. doi:10.1016/j.cosrev.2024.100658.

Lee, H., Kwon, H., 2022. Self-supervised contrastive learning for cross-domain hyperspectral image representation, in: *Proc. IEEE Int. Conf. Acoust. Speech Signal Process. (ICASSP)*, pp. 3239–3243. doi:10.1109/ICASSP43922.2022.9747010.

Li, Z., Liu, M., Chen, Y., Xu, Y., Du, Q., 2022. Deep cross-domain few-shot learning for hyperspectral image classification. *IEEE Trans. Geosci. Remote Sens.* 60, 1–18. doi:10.1109/TGRS.2021.3057066.

Li, Z., Xu, Q., Ma, L., Fang, Z., Wang, Y., He, W., Du, Q., 2023. Supervised contrastive learning-based unsupervised domain adaptation for hyperspectral image classification. *IEEE Trans. Geosci. Remote Sens.* 61, 1–17. doi:10.1109/tgrs.2023.3317301.

Li, Z., Xue, Z., Jia, M., Nie, X., Wu, H., Zhang, M., Su, H., 2024. Demae: Diffusion-enhanced masked autoencoder for hyperspectral image classification with few labeled samples. *IEEE Trans. Geosci. Remote Sens.* 62, 1–16. doi:10.1109/TGRS.2024.3445991.

Liang, M., Wu, W., Shen, H., Yu, L., Yu, X., Jiao, L., 2025. Supercot-x: Masked hyperspectral image modeling with diverse superpixel-level contrastive tokenizer. *IEEE J. Sel. Topics Appl. Earth Obs. Remote Sens.* .

Lin, J., Gao, F., Shi, X., Dong, J., Du, Q., 2023. Ss-mae: Spatial-spectral masked autoencoder for multisource remote sensing image classification. *IEEE Trans. Geosci. Remote Sens.* 61, 1–14. doi:10.1109/TGRS.2023.3331717.

Liu, B., Gao, K., Yu, A., Ding, L., Qiu, C., Li, J., 2022. ES²FL: Ensemble self-supervised feature learning for small sample classification of hyperspectral images. *Remote Sens.* 14, 4236. doi:10.3390/rs14174236.

Liu, H., Zhang, M., Di, Z., Gong, M., Gao, T., Qin, A.K., 2024. A hybrid multitask learning network for hyperspectral image classification with few labels. *IEEE Trans. Geosci. Remote Sens.* 62, 1–16. doi:10.1109/TGRS.2024.3356008.

Liu, W., Liu, K., Sun, W., Yang, G., Ren, K., Meng, X., 2023. Self-supervised feature learning based on spectral masking for hyperspectral image classification. *IEEE Trans. Geosci. Remote Sens.* 61, 1–15. doi:10.1109/TGRS.2023.3310489.

Long, M., Cao, Y., Wang, J., Jordan, M., 2015. Learning transferable features with deep adaptation networks, in: International conference on machine learning, PMLR. pp. 97–105.

Makantasis, K., Karantzalos, K., Doulamis, A., Doulamis, N., 2015. Deep supervised learning for hyperspectral data classification through convolutional neural networks, in: Proc. IEEE Int. Geosci. Remote Sens. Symp. (IGARSS), IEEE. pp. 4959–4962.

Pan, B., Shi, Z., Xu, X., 2017. Mugnet: Deep learning for hyperspectral image classification using limited samples. *ISPRS Open J. Photogramm. Remote Sens.* 145, 108–119.

Paoletti, M.E., Haut, J.M., Plaza, J., Plaza, A., 2019. Deep learning classifiers for hyperspectral imaging: A review. *ISPRS J. Photogramm. Remote Sens.* 158, 279–317. doi:10.1016/j.isprsjprs.2019.09.006.

Polewski, P., Yao, W., Heurich, M., Krzystek, P., Stilla, U., 2016. Combining active and semisupervised learning of remote sensing data within a renyi entropy regularization framework. *IEEE J. Sel. Topics Appl. Earth Observ. Remote Sens.* 9, 2910–2922.

Qin, B., Feng, S., Zhao, C., Li, W., Tao, R., Xiang, W., 2024. Cross-domain few-shot learning based on feature disentanglement for hyperspectral image classification. *IEEE Trans. Geosci. Remote Sens.* 62, 1–15. doi:10.1109/TGRS.2024.3386256.

Shi, C., Fang, L., Lv, Z., Zhao, M., 2022. Explainable scale distillation for hyperspectral image classification. *Pattern Recognit.* 122, 108316.

Song, Y., Zhang, J., Liu, Z., Xu, Y., Quan, S., Sun, L., Bi, J., Wang, X., 2025. Deep learning for hyperspectral image classification: A comprehensive review and future predictions. *Inf. Fusion* 123, 103285. doi:10.1016/j.inffus.2025.103285.

Thota, M., Leontidis, G., 2021. Contrastive domain adaptation, in: Proc. IEEE Conf. Comput. Vis. Pattern Recognit., IEEE. doi:10.1109/CVPRW53098.2021.00250.

Tu, L., Li, J., Huang, X., Gong, J., Xie, X., Wang, L., 2024. S^2HM^2 : A spectral-spatial hierarchical masked modeling framework for self-supervised feature learning and classification of large-scale hyperspectral images. IEEE Trans. Geosci. Remote Sens. 62, 1–19. doi:10.1109/TGRS.2024.3392962.

Wambugu, N., Chen, Y., Xiao, Z., Tan, K., Wei, M., Liu, X., Li, J., 2021. Hyperspectral image classification on insufficient-sample and feature learning using deep neural networks: A review. Int. J. Appl. Earth Obs. Geoinf. 105, 102603. doi:10.1016/j.jag.2021.102603.

Wang, P., Yao, W., 2022. A new weakly supervised approach for als point cloud semantic segmentation. ISPRS J. Photogramm. Remote Sens. 188, 237–254.

Wang, P., Yao, W., Shao, J., He, Z., 2025. Test-time adaptation for geospatial point cloud semantic segmentation with distinct domain shifts. ISPRS J. Photogramm. Remote Sens. 229, 422–435.

Wang, X., Liu, J., Chi, W., Wang, W., Ni, Y., 2023. Advances in hyperspectral image classification methods with small samples: A review. Remote Sens. 15, 3795. doi:10.3390/rs15153795.

Wu, H., Shi, C., Yue, S., Zhu, F., Jin, Z., 2025. Domain adaptation network based on multi-level feature alignment constraints for cross scene hyperspectral image classification. Knowledge-Based Systems 325, 113972. doi:10.1016/j.knosys.2025.113972.

Xi, B., Zhang, Y., Li, J., Li, Y., Li, Z., Chanussot, J., 2024. Ctf-sscl: Cnn-transformer for few-shot hyperspectral image classification assisted by semisupervised contrastive learning. IEEE Trans. Geosci. Remote Sens. 62, 1–17. doi:10.1109/TGRS.2024.3465225.

Zhang, B., Zhao, L., Zhang, X., 2020. Three-dimensional convolutional neural network model for tree species classification using airborne hyperspectral images. Remote Sens. Environ. 247, 111938. doi:10.1016/j.rse.2020.111938.

Zhang, X., Han, L., 2023. A generic self-supervised learning (ssl) framework for representation learning from spectral–spatial features of unlabeled remote sensing imagery. *Remote Sens.* 15, 5238. doi:10.3390/rs15215238.

Zhang, Y., Zhang, Q., Liu, W., 2025. Open set domain adaptation via unknown construction and dynamic threshold estimation. *Neurocomputing* 648, 130668. doi:10.1016/j.neucom.2025.130668.

Zhao, C., Zhu, W., Feng, S., 2022. Superpixel guided deformable convolution network for hyperspectral image classification. *IEEE Trans. Image Process.* 31, 3838–3851.

Zhong, Z., Li, Y., Ma, L., Li, J., Zheng, W.S., 2022. Spectral–spatial transformer network for hyperspectral image classification: A factorized architecture search framework. *IEEE Trans. Geosci. Remote Sens.* 60, 1–15. doi:10.1109/TGRS.2021.3115699.

Zhou, F., Wang, P., Zhang, L., Wei, W., Zhang, Y., 2023. Revisiting prototypical network for cross domain few-shot learning, in: Proc. IEEE/CVF Conf. Comput. Vis. Pattern Recognit. (CVPR), pp. 20061–20070.